ACS OMEGA

http://pubs.acs.org/journal/acsodf

Article

Comprehensive Model for the Synthesis of γ-Al_2O_3 Microsphere-Supported Bimetallic Iron- and Copper Oxide Materials

Bram Seynnaeve,* Jeroen Lauwaert, Pascal Van Der Voort, and An Verberckmoes

Cite This: *ACS Omega* 2022, 7, 41796−41803

Read Online

ACCESS | Metrics & More | Article Recommendations | Supporting Information

ABSTRACT: The effects of incipient wetness impregnation synthesis conditions on the macro- and microscopic properties of bimetallic iron oxide/copper oxide@γ-Al_2O_3 microspheres were elucidated. The key steering factors for the macroscopic distribution of the metals throughout the support, and for the metal nanoparticle sizes, were the pH of the impregnation solution, the counterions present in the metal precursor, the amount of negatively charged groups on the alumina, the complexation of iron, the impregnation strategy (simultaneous or sequential) and, in the latter case, the order of impregnation. The interactions taking place during impregnation are identified as competitive adsorption of charged dissolved species (Fe/Cu cations, protons, and additional anions) in the impregnation solution. Adsorption can take place on either charged alumina sites or previously deposited metal (i.e., iron on iron, copper on copper, iron on copper, and copper on iron) and is affected by counterion shielding. Modeling of these interactions via simulation on an in-house-developed python code allowed quantification of the adsorption constants for each of the above-mentioned processes, where iron adsorbs much faster than copper on all surfaces, and adsorption of iron on both alumina surface groups and previously deposited copper contributes majorly to the final iron distribution. The findings in this work will allow for better prediction and control over bimetallic materials synthesized via the simple and scalable impregnation procedure.

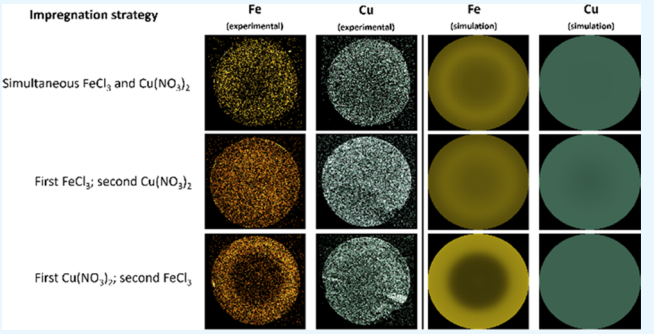

1. INTRODUCTION

Supported metal-based nanoparticles are prominently used in many fields such as adsorption, drug delivery, bioimaging, and catalysis.[1,2] Both in application and research, much attention has been given to nanoparticle structures that combine multiple metals in a single material. The performance of such bimetallic nanoparticle materials in an application may strongly differ from their monometallic counterparts, as they can exhibit unique electronic, thermal, optical, and catalytic properties. These bimetallic materials can be prepared in different arrangements, the most common being alloys, core−shell, and contact aggregates. Each of these arrangements allows specific interactions between the metals. Moreover, which metals are accessible to the environment (only one or both) is strongly dependent on their arrangement.[3,4] Various interaction processes can occur between the two metals, and related to catalysis, these are (i) synergy, when both metals participate as catalysts and potentially allow alternative reaction pathways; (ii) geometric modification, where the presence of the second metal alters the geometry of the catalytically active metal; (iii) electronic effects, when electron transfer between the two metals occurs; (iv) stabilization, when the function of the second metal is related to the enhancement of the durability of the catalytically active metal (e.g., by decreasing metal leaching by providing a stable binding site for the other metal, or by adsorbing compounds that could deactivate the active metal). As such, the presence of a second metal can improve the catalytic performance of a material, by increasing the activity, fine-tuning the selectivity, or enhancing the stability.[5]

The synthesis of supported bimetallic nanoparticle materials is more complex than that of monometallic materials as interactions can occur between the different metals during synthesis, and often additional synthesis steps are needed to make the final materials. This increased complexity often results in ill-defined particles with varying sizes and inhomogeneous distributions and compositions. Some research on bimetallic materials does employ relatively simple and scalable synthesis methods such as impregnation and controlled surface reactions.[6−8] However, in academic settings, more complex synthesis techniques such as atomic layer deposition (ALD), electrochemical deposition (ED), colloidal/

Received: September 28, 2022
Accepted: October 6, 2022
Published: October 31, 2022

https://doi.org/10.1021/acsomega.2c06273
ACS Omega 2022, 7, 41796−41803

polyol synthesis, and laser ablation are frequently used.[9−11] While these techniques more reliably achieve small particle sizes and well-defined metal compositions, their complex instrumental setup (in cases such as ALD and ED) or more involved synthesis procedure steps (polyol synthesis) often make them (a) difficult to scale up to industrial settings and (b) not always ideal for the preparation of supported particles.[12,13] As such, an improved understanding of how to obtain enhanced control over the properties of supported bimetallic nanoparticles using more scalable methods is of great value.[14]

In a previous publication, we gave insight into the processes taking place during the impregnation synthesis of a single metal salt, either a copper or an iron salt, into a γ-alumina microsphere support.[15] Strong attractive interactions between the charged alumina surface and dissolved ionic metal species were found to cause early deposition of the metal, resulting in inhomogeneous distributions on the metal. Of note was the occurrence of competitive adsorption between the positive metal ions and other cations present in the solution, giving rise to particularly complex metal distribution profiles with several zones with higher and lower metal concentrations (leading to either egg-shell, egg-yolk, or egg-white distributions). The strength of attractive interactions between the support surface and dissolved species was found to be the main determining factor. As γ-Al_2O_3 was used as support material, the number of charged surface sites, as described by the point of zero charge (PZC), is the most important factor. The electronic charge of alumina depends on the state of the hydroxyl groups on the alumina surface, which can be positively, negatively, or not charged. At default, the surface will be at its PZC, but via interactions with solutions with a pH lower or higher than the PZC value, the surface groups will be protonated or deprotonated, respectively.[16,17] For γ-Al_2O_3, the PZC value is typically around 7−9, so a net adsorption of protons can be expected in contact with solutions with a pH below this value, which will result in a decrease of negatively charged surface groups and an increase in positively charged groups on the alumina surface. For copper, the interactions between the charged surface groups of the support and the dissolved metal ions are sufficiently weak to avoid early deposition during the impregnation step, resulting in a fully homogeneous distribution of the metal under the form of a coating. Conversely, iron showed a strong interaction with the alumina surface, resulting in early adsorption of the metal, with competitive adsorption with other positive ions such as H^+. This early deposition of iron could be mitigated by reducing the interactions between the dissolved iron and alumina surface, by adding a sufficient concentration of H^+ to the precursor, by modifying the electronic charge of the alumina surface, or by complexation of the iron ions with citrate ligands. Modeling the interactions occurring during impregnation synthesis allowed for accurate prediction of the metal distribution for monometallic iron and copper materials on porous γ-alumina microspheres, enabling more controlled synthesis of materials with specific desired metal distributions.

To extend the above-described insights to bimetallic systems, the model developed for monometallic materials should be extended to include several new interactions: the competitive adsorption of multiple metals, the increased or decreased deposition of one metal on previously deposited metal (e.g., deposition of iron on previously deposited copper) compared to deposition on the support surface. Additionally, the potential deposition of a metal on itself (e.g., deposition of iron on previously deposited iron) should also be taken into account in the new model. Systematic synthesis of bimetallic catalysts via incipient wetness impregnation will provide the experimental basis on which to develop the model. Therefore, bimetallic iron oxide/copper oxide materials are synthesized both by simultaneous impregnation of both metals in a single precursor solution and by sequential impregnation where first a single metal solution is brought into the support, after drying and calcination followed by impregnation of the second metal. This sequential method can be performed in both possible impregnation orders. Hence, modeling of the bimetallic iron oxide and copper oxide particles in the porous γ-alumina microspheres allows us to quantify and simulate the observed distributions. The insights gained into the processes taking place during impregnation synthesis, and their relative importance, allow us to predict the physical properties of the resulting bimetallic materials, enhancing the control over these complex materials.

2. MATERIALS AND METHODS

2.1. Synthesis Procedure. The iron and copper precursors used for the impregnation procedures were iron(III)nitrate nonahydrate ($Fe(NO_3)_3{\cdot}9H_2O$), iron(III)-chloride ($FeCl_3$), iron(III)citrate ($C_6H_5FeO_7$), and copper-(II)nitrate hemipentahydrate ($Cu(NO_3)_2{\cdot}2.5H_2O$), as purchased from Sigma-Aldrich. The support materials were 1.8 mm (diameter) PURALOX γ-Al_2O_3 microspheres from SASOL (product code 604130).

Two strategies were employed to synthesize the bimetallic iron oxide/copper oxide materials, both based on the incipient wetness procedure described in earlier research.[15] In both strategies, the alumina microspheres are dried at 120 °C for 8 h prior to impregnation. During the impregnation step, aqueous metal solution equal to the pore volume of the support is added dropwise to the support to maintain incipient wetness conditions and left to equilibrate for 3 h. During the drying and calcinating steps, the material is heated in a muffle furnace (Naber-therm Lx/11) at a rate of 1 °C min^{-1} and dried in air at 120 °C for 12 h and calcined at 450 °C for 4 h (at a heating rate of 5 °C min^{-1}). In the first strategy, the selected iron and copper salts and potential additives (e.g., HCl) were dissolved in a single solution. The materials synthesized by this method are denoted as "Sim_{iron precursor + acid additive if any}_{copper precursor}" (e.g., Sim_$FeCl_3$ + HCl_$CuNO_3$). In the second strategy, the metals were impregnated sequentially, with one metal salt solution being impregnated first, followed by drying and calcination to the oxide form, after which the second metal is impregnated in the calcined material, followed by a second drying and calcination procedure. These materials are denoted as "Seq_{precursor used in first step + acid additive if any}_{precursor used in second step + acid additive if any}" (e.g., Seq_$CuNO_3$_$FeNO_3$). For two materials, the alumina support (or the copper-containing material after the first impregnation step) was pretreated with a solution of 3 M HCl prior to impregnation with $FeCl_3$, to reduce the number of negatively charged alumina surface species present in the support. For this, an incipient wetness volume of a 3 M HCl solution was added dropwise to the microspheres, and after 2 h of contact time at room temperature, the microspheres were again dried at 120 °C for 8 h. In these cases, the iron precursor is denoted as "HCl-pretreatement+$FeCl_3$." In all cases, the concentrations of the employed iron and copper precursor

https://doi.org/10.1021/acsomega.2c06273
ACS Omega 2022, 7, 41796−41803

solutions were prepared aiming at materials with a load of 5 wt % iron and 5 wt % copper, present under the metal oxide form. The concentration of the utilized precursor solutions was calculated as follows: the bimetallic material with 5 wt % of Fe and 5 wt % of Cu will have a wt $\%_{Fe_2O_3}$ and wt $\%_{CuO}$ of

$$\text{wt }\%_{Fe_2O_3} = 5\%*\frac{MM_{Fe_2O_3}}{2*MM_{Fe}} = 7.15 \text{ wt }\% \quad (1)$$

$$\text{wt }\%_{CuO} = 5\%*\frac{MM_{CuO}}{MM_{Cu}} = 6.26 \text{ wt }\% \quad (2)$$

The total mass of the final material (consisting of the alumina support, Fe_2O_3, and CuO) will have a total mass of

$$m_{total} = 100*\frac{m_{support}}{100 - \text{wt }\%_{Fe_2O_3} - \text{wt }\%_{CuO}} = 1.155*m_{support} \quad (3)$$

and so the molar amounts of Fe_2O_3 and CuO in the final material are

$$n_{Fe_2O_3} = \frac{m_{total}*\text{wt }\%_{Fe_2O_3}}{MM_{Fe_2O_3}} \quad (4)$$

$$n_{CuO} = \frac{m_{total}*\text{wt }\%_{CuO}}{MM_{CuO}} \quad (5)$$

The corresponding molar amount of $Fe(NO_3)_3{\cdot}9H_2O$, ferric ammonium citrate, or $Cu(NO_3)_2{\cdot}2.5H_2O$ is measured and dissolved in an incipient wetness volume of water, which was experimentally determined to be

$$1.03\frac{mL}{g}*m_{support} \quad (6)$$

Finally, in the case of $Fe(NO_3)_3{\cdot}9H_2O$ and $Cu(NO_3)_2{\cdot}2.5H_2O$, the presence of the crystal water should be taken into account, lowering the amount of water added to create the precursor solution to

$$1.03\frac{mL}{g}*m_{support} - n_{metal}*X*MM_{H_2O} \quad (7)$$

where X is 9 for $Fe(NO_3)_3{\cdot}9H_2O$ and 2.5 for $Cu(NO_3)_2{\cdot}2.5H_2O$. These calculations result in the concentrations shown in Table 1.

Table 1. Concentrations of All Used Iron and Copper Precursors as Used to Synthesize 5 wt % iron/5 wt % Copper Bimetallic Materials

metal salt used in solution	concentration (M)
$Cu(NO_3)_2{\cdot}2.5H_2O$	0.919
$Fe(NO_3)_3{\cdot}9H_2O$	1.199
Fe(III)citrate	1.003

2.2. Characterization. The iron and copper loadings of all samples were determined using inductively coupled plasma-optical emission spectroscopy (ICP-OES) on a Thermo iCAP 7000 radial instrument, with a wavelength of 259.940 nm for iron and 324.754 nm for copper. The analyzed solutions were prepared by dissolving 50 mg of material using a microwave treatment (Milestone Ultrawave ECR) at 270 °C, 120 bar in 9 M HCl and 4 M HNO_3.

For the determination of the crystal phases present in each sample, powder X-ray diffraction (PXRD) measurements were performed on a Thermo Scientific ARL X'TRA Powder Diffractometer employing Cu Kα radiation. Prior to the measurement, the microsphere samples were ground to a fine powder.

The macroscopic distribution of the metals throughout the support and composition of the formed nanoparticles were measured with scanning electron microscopy−energy-dispersive X-ray spectroscopy (SEM−EDX) measurements, performed using a JEOL JSM-5600 instrument with a 15 keV electron beam, where the secondary electron signal was used to construct the SEM images, and the characteristic X-rays to construct the EDX mappings. For these measurements, the support spheres were cut in halves, to perform the measurements on the full depth on the support. To examine the distribution of iron and copper on the alumina in more detail, additional scanning transmission electron microscopy−energy-dispersive X-ray spectroscopy (STEM-EDX) measurements were taken with a JEOL JEM-2200FS HR (S)TEM apparatus, on materials ground to a fine powder prior to analysis.

2.3. Modeling. The model for simulating the processes taking place during impregnation synthesis is a more refined version of the in-house-developed Python code fully described in our previous work.[15] As in the previous work, program simulates the impregnation by considering the adsorption of dissolved species (metal species, protons, and counterions) on charged alumina surface groups to be described by a second-order reaction with an adsorption rate constant k, so the adsorption rate r_{ads} is given by

$$r_{ads} = k*c_{surface\ group}*c_{dissolved\ species} \quad (8)$$

The additional interactions that are taken into account are the adsorption of a dissolved metal on previously deposited metal, also modeled as a second-order reaction with an adsorption rate of

$$r_{ads} = k*c_{dissolved\ metal}*c_{deposited\ metal} \quad (9)$$

where k is the adsorption rate constant, $c_{dissolved\ metal}$ is the local concentration of a dissolved metal (iron or copper), and $c_{deposited\ metal}$ is the surface concentration of a deposited metal (iron or copper) at the same place. Each possible metal-on-metal adsorption is characterized by its own adsorption rate constant k, resulting in four new parameters being introduced in the model: $k_{Cu\ on\ Cu}$, $k_{Fe\ on\ Fe}$, $k_{Cu\ on\ Fe}$, and $k_{Fe\ on\ Cu}$. These new parameters, together with parameters from the original model (which were the adsorption constants of dissolved species on alumina: K_{Cu}, K_{Fe}, K_H, K_{Cl}, K_{NO_3}; shielding constants for Cl^- and NO_3^-; and the proportion of positively charged alumina surface groups $\theta+$) were all optimized via a gradient descent algorithm minimizing the sum of residual quadratic errors between the experimental distributions observed via EDX, and the modeled distributions.

3. RESULTS AND DISCUSSION

Table 2 shows the 17 materials synthesized: alumina loaded with 5% $Cu(NO_3)_2$ as copper salt and $Fe(NO_3)_3$, $FeCl_3$, or ferric ammonium citrate as iron salt, samples with acidified iron precursors (either $FeCl_3$ + 3M HCl or $Fe(NO_3)_3$ + 3M HNO_3) and samples created from HCl-pretreated alumina supports. All of these samples were synthesized with both the simultaneous impregnation method and the sequential

https://doi.org/10.1021/acsomega.2c06273
ACS Omega 2022, 7, 41796−41803

Table 2. Overview of All 17 Bimetallic Iron Oxide/Copper Oxide@γ-Al_2O_3 Materials

Sim_$FeCl_3$_$Cu(NO_3)_2$	Sim_$Fe(NO_3)_3$ + HNO_3_$Cu(NO_3)_2$
Seq_$FeCl_3$_$Cu(NO_3)_2$	Seq_$Fe(NO_3)_3$ + HNO_3_$Cu(NO_3)_2$
Seq_$Cu(NO_3)_2$_$FeCl_3$	Seq_$Cu(NO_3)_2$_$Fe(NO_3)_3$ + HNO_3
Sim_$Fe(NO_3)_3$_$Cu(NO_3)_2$	Sim_FeCitrate_ $Cu(NO_3)_2$
Seq_$Fe(NO_3)_3$_$Cu(NO_3)_2$	Seq_FeCitrate_ $Cu(NO_3)_2$
Seq_$Cu(NO_3)_2$_$Fe(NO_3)_3$	Seq_$Cu(NO_3)_2$_FeCitrate
Sim_$FeCl_3$ + HCl_ $Cu(NO_3)_2$	Seq_HCl-pretreatement + $FeCl_3$_$Cu(NO_3)_2$
Seq_$FeCl_3$ + HCl_ $Cu(NO_3)_2$	Seq_$Cu(NO_3)_2$_HCl-pretreatement + $FeCl_3$
Seq_ $Cu(NO_3)_2$_$FeCl_3$+HCl	

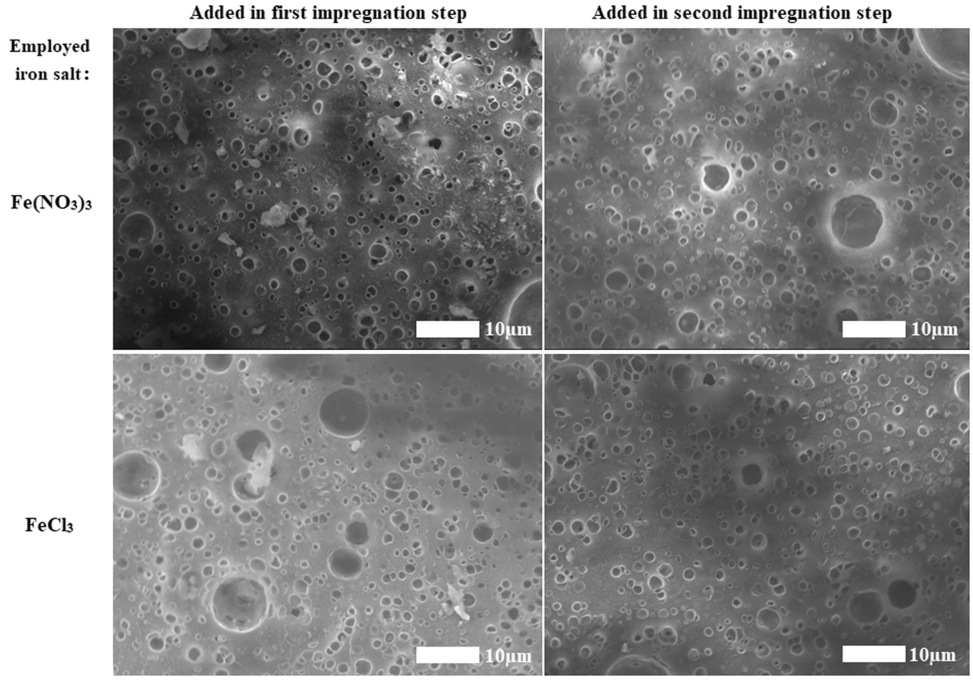

Figure 1. SEM images of the interior of four materials synthesized with sequential impregnation, clearly showing the difference in cluster formation between materials where iron was impregnated as the first metal (left) and those where copper was impregnated first (right).

impregnation in both orders. With exception of the HCl-pretreated materials, where simultaneous impregnation was not performed since this synthesis resulted in damage of the support material during the calcination step. The iron and copper loading of each material, as determined using ICP-OES, can be found in the Supporting Information (Table S1). The measurements revealed the actual iron and copper loadings of the materials to be systematically slightly lower than the expected 5 wt %, usually in the 4.5−5% range. In a few cases, the iron loading is significantly lower (in the 3−4 wt % range). This is most notable in the samples prepared with the ammonium ferric citrate precursor and is most likely caused by the relatively high viscosity of this precursor.

The XRD patterns of the samples (Figures S1−S5) show that the crystalline fractions formed in the final materials depend mostly on which iron salt (and modification method) was used during impregnation synthesis. The samples synthesized with $FeNO_3$ show clear diffractions at 33.1, 36.0, 49.8, and 54.5° and smaller diffractions at 41.1, 62.7, and 64.2°; these diffractions can be attributed to the presence of α-Fe_2O_3 (JCPDS: 86-0550). These exact same diffractions are also found in the three samples synthesized with the $FeNO_3$ + 3M HNO_3 precursor. All three samples prepared with the unmodified $FeCl_3$ precursor feature a small diffraction at 16.2°, and two more pronounced diffractions at 32.4 and 39.6°, although no iron or copper compound that matches with these diffractions could be found. These three diffractions are most distinct in the case where $FeCl_3$ was impregnated as second metal and least distinct in the case where $FeCl_3$ was the first metal. These same three diffractions are also clearly visible in the HCl-pretreated sample where $FeCl_3$ was added in the second step, but not in the HCl-pretreated sample with $FeCl_3$ impregnated in the first step, where no clear diffractions are present. As such, these diffractions are most likely related to an iron chloride and/or oxide compound that is removed during the additional calcination step. Finally, the materials prepared with the ammonium ferric citrate precursor feature no distinguishable diffractions, indicating the absence of significant amounts of crystalline phases.

SEM images (Figure 1) show that the nanoparticle sizes are both influenced by the choice of impregnation precursor and by the order of impregnation. In general, unmodified $FeNO_3$ precursors resulted in the formation of large, cluster-like particles. These particles were also present to a lesser extent in $FeCl_3$ samples and completely absent in iron citrate samples. For both $FeNO_3$- and $FeCl_3$-based materials, the clusters were most present in the materials where the iron salt was added as the first metal and least present when iron was added as the second metal, indicating that the presence of copper oxide seems to decrease the tendency of iron oxide to cluster

https://doi.org/10.1021/acsomega.2c06273
ACS Omega 2022, 7, 41796−41803

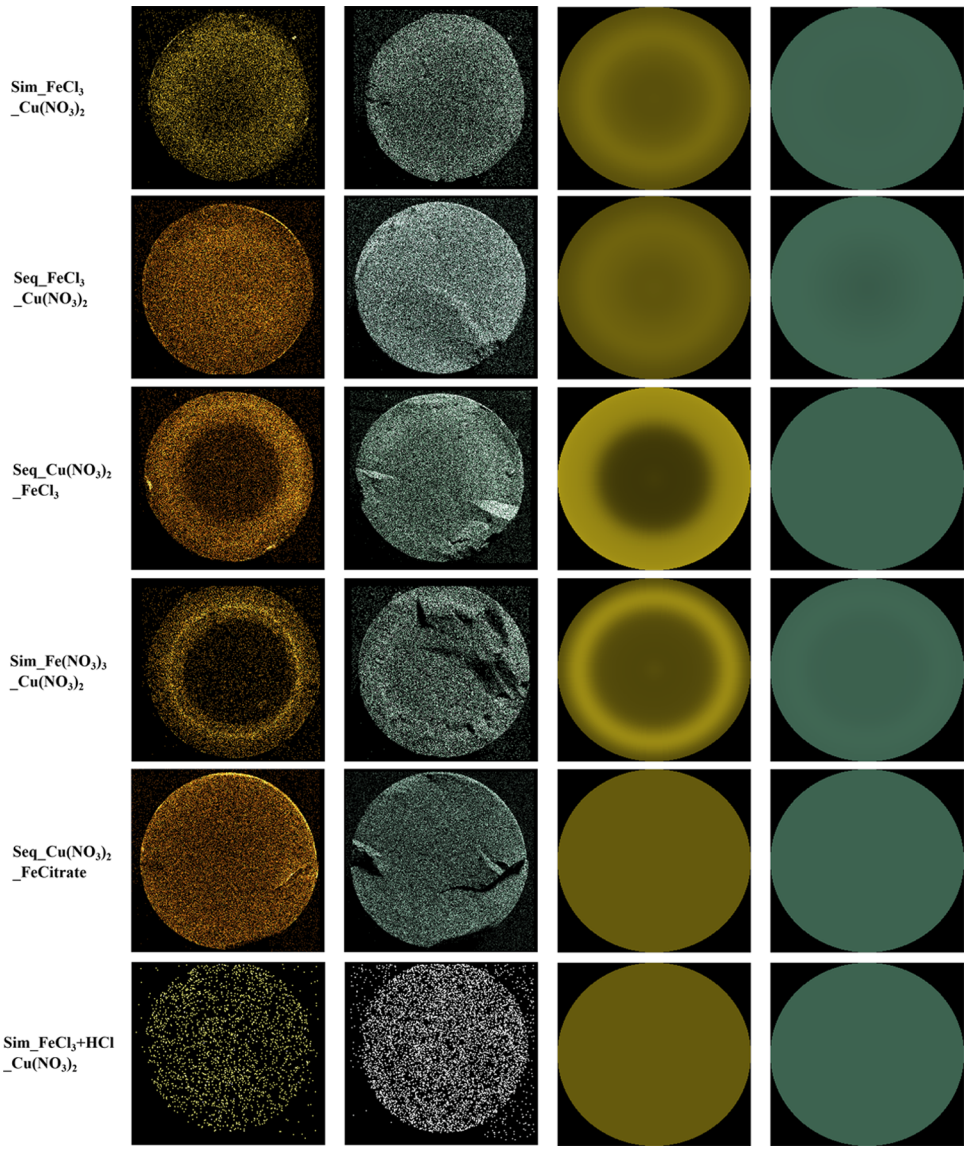

Figure 2. SEM−EDX mappings of iron and copper throughout the spherical support (left) and the predicted iron and copper distributions according to the simulation (right), for the following selected samples (from top to bottom): samples impregnated with $FeCl_3$ as iron precursor for all three synthesis strategies (simultaneous, iron in the first step and iron in the second step), a sample made with $Fe(NO_3)_3$ precursor, a sample made with ferric ammonium citrate, and a sample made with an acidified iron precursor solution. The set of all materials can be found in Figure S6.

together. Additional STEM-EDX measurements of alumina flakes from ground samples (Figure S7) confirm that in sequential impregnation, the metals deposit on top of each other: in thin parts of the flakes (with lighter color), corresponding to alumina on which only a small amount of metal has been deposited, the first added metal is more abundant. Meanwhile, on sections that include more of the deposited metals (with darker color), the second metal is more abundant, showcasing clear growth of the secondly deposited metal oxide on top of the first deposited metal oxide.

Figure 2 (left) shows the macroscopic iron and copper distribution throughout the support microspheres in a selection of the synthesized materials. The overview of all synthesized materials can be found in the Supporting Information (Figure S6, left). In the cases of sequential impregnation, the images show that the impregnation of the second material is being affected by the presence of the first deposited metal. This is most pronounced for the materials where a noncomplexed iron salt ($Fe(NO_3)_3$ or $FeCl_3$) was impregnated in the second step, as in these materials, the presence of iron is limited to the exterior regions of the support. This decrease in impregnation depth is less present for the citrate-complexed samples, where almost fully homogeneous iron distributions were obtained. In the cases where $Cu(NO_3)_2$ was impregnated in the second step, iron is distributed according to patterns found for monometallic iron (inhomogeneous bands for $Fe(NO_3)_3$ and $FeCl_3$; homogeneous for iron citrate), while the copper distributions remained homogeneous despite the presence of iron, indicating no strong deposition of copper on the iron nanoparticles. The iron distributions encountered during simultaneous impregnation are intermediate between these found for sequential impregnation, indicating the iron deposition is affected by the copper which has already been deposited during the impregnation step.

https://doi.org/10.1021/acsomega.2c06273
ACS Omega 2022, 7, 41796−41803

Our previous publication[15] showed that the distribution of iron can be made more homogeneous by (i) lowering the pH of the used impregnation solution or by (ii) pretreating the alumina support with an acidic solution. Upon assessing both modified synthesis methods in the preparation of γ-Al_2O_3-supported bimetallic iron- and copper oxide materials, homogeneous iron distributions were obtained for all cases where iron was added simultaneously with copper or when iron was added as the first metal (Figure S6, rows 9−13). However, in cases where iron was the second impregnated metal, nonhomogeneous distributions were obtained for iron, and even the copper distributions have become slightly inhomogeneous (Figure S6, rows 14 and 15). The iron distributions in these latter samples featured a higher iron concentration in the center of the support spheres, which is the opposite for the inhomogeneous distributions found for the nonmodified samples. These effects can be explained due to the high amounts of acid present in the precursors, which might redissolve the copper oxide already present in the sample. This dissolved copper will travel in the direction of the impregnating solution, resulting in a net movement of copper from the exterior of the support toward the interior of the support. As already demonstrated, iron will preferentially deposit on copper, resulting in increased deposition of iron in the copper-rich center. Because the model used in this paper does not take the possibility of this redissolving of copper into account, it cannot properly predict the samples where strong acids are used in the second step of a sequential impregnation.

The model developed to describe the impregnation process was trained on the EDX mappings of the bimetallic materials, as well as the metal distributions of the monometallic samples described in previous work.[15] Figure 2 (right) shows the iron and copper distributions for selected materials, as predicted by the model. The complete set of predicted distributions of all materials can be found in Figure S6 (right). Table 3 shows an overview of the estimated model parameters, which are the shielding factors of the counterions (Cl and NO_3), adsorption rate constants of each component on alumina surface groups (k_{Fe}, k_{Cu}, k_H, k_{Cl}, k_{NO_3}), the fraction of positively charged surface sites (θ_+) and the newly introduced adsorption rate constants of dissolved metal species on deposited metals (k_{FeOnFe}, k_{CuOnCu}, k_{FeOnCu}, k_{CuOnFe}).

Table 3. Estimated Values of the Model Parameters and Their 95% Confidence Intervals

model parameter	estimated value	95% confidence interval (% of value)
shielding factor Cl^-	8.70×10^{-6}	$\pm 5.55 \times 10^{-7}$ (6.38%)
shielding factor NO_3^-	6.50×10^{-7}	$\pm 2.96 \times 10^{-8}$ (4.55%)
kFe^{3+}(mol s^{-1})	0.23×10^{0}	$\pm 8.23 \times 10^{-4}$ (0.36%)
kCu^{2+}(mol s^{-1})	1.73×10^{-12}	$\pm 7.63 \times 10^{-13}$ (44.12%)
kH^+(mol s^{-1})	1.52×10^{0}	$\pm 8.19 \times 10^{-4}$ (0.05%)
kCl^-(mol s^{-1})	7.04×10^{0}	$\pm 0.39 \times 10$ (5.51%)
kNO_3^-(mol s^{-1})	5.54×10^{-4}	$\pm 2.13 \times 10^{-5}$ (3.84%)
θ_+ (for nontreated support)[a]	46.0%	±0.253 (0.55%)
θ_+ (for 3 M HCl-pretreated support)	91.9%	±4.43 (4.82%)
kFeOnFe (mol s^{-1})	7.93×10^{-3}	$\pm 1.45 \times 10^{-3}$ (13.75%)
kCuOnCu (mol s^{-1})	1.16×10^{-7}	$\pm 7.97 \times 10^{-8}$ (68.71%)
kFeOnCu (mol s^{-1})	6.17×10^{-2}	$\pm 8.22 \times 10^{-4}$ (1.33%)
kCuOnFe (mol s^{-1})	1.15×10^{-3}	$\pm 8.18 \times 10^{-5}$ (7.11%)

[a] θ_+ is the fraction of the total surface sites that are positively charged; the fraction of negatively charged surface sites is $(1 - \theta_+)$.

It is important to note that the model allows two distinct ways for the metal to deposit early during impregnation: either by adsorption on the alumina surface or by adsorption on previously deposited metal. As such, the adsorption rate constants of iron and copper on alumina are lower than previously reported,[15] as a share of the adsorption takes place under the form of metal-on-metal adsorption, which was not accounted for in the previous version of the model. In the case of iron adsorption, adsorption on the alumina surface is still the fastest (K_{Fe} = 0.23) although adsorption on copper also plays a significant role ($K_{FeOnCu} = 6.17 \times 10^{-2}$), the contribution of the adsorption of iron species on deposited iron is relatively minor ($K_{FeOnFe} = 7.93 \times 10^{-3}$). For copper, the adsorption on alumina is very slow ($K_{Cu} = 1.73 \times 10^{-12}$) and is insignificant compared to the adsorption of copper on previously deposited iron ($K_{CuOnFe} = 1.15 \times 10^{-3}$). The previously observed trend of iron adsorbing more strongly than copper still holds, both for metal on alumina adsorption (K_{Fe} = 0.23, $K_{Cu} = 1.73 \times 10^{-12}$) and for metal on metal adsorption ($K_{FeOnFe} = 7.93 \times 10^{-3}$; $K_{CuOnFe} = 1.15 \times 10^{-3}$; $K_{FeOnCu} = 6.17 \times 10^{-2}$; $K_{CuOnCu} = 1.16 \times 10^{-7}$).

Based on the model, an improved mechanistic explanation of the processes taking place during impregnation synthesis can be given, as shown in Figure 3. The scheme represents an

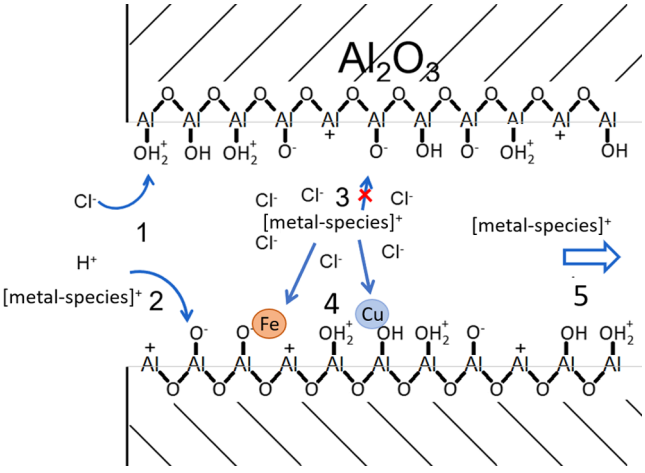

Figure 3. Detailed schematic representation of the processes taking place during impregnation synthesis: (1) adsorption of charged dissolved species on alumina surface groups with opposite charge, in the case of multiple species with the same type of charge this adsorption is competitive (2). Anions shielding the dissolved metal from interacting (3). The dissolved metal adsorbing on previously deposited iron or copper species (4). Nondeposited metal remaining in solution in the alumina pores (5), until evaporation of the solvent.

impregnation synthesis, where a precursor solution containing dissolved metal (Fe and/or Cu) species, dissolved counter anions (Cl^- or NO_3^-), and protons is brought into the alumina support. Here, the adsorption of charged dissolved species on surface groups with opposite charge (1) occurs. In the case of multiple species with the same charge, there will be competition for the charged surface sites (2), where $K_{Cl} > K_{H^+} > K_{Fe} > K_{NO_3} > K_{Cu}$. The electrostatic shielding of anionic species around the metal cations (3), where the shielding effect of Cl^- is much larger than that of NO_3^-. This electrostatic shielding affects both the adsorption of dissolved metal onto

https://doi.org/10.1021/acsomega.2c06273
ACS Omega 2022, 7, 41796−41803

the alumina surface and the adsorption of previously deposited metal species (4). This metal-on-metal adsorption process can occur on either deposited metal, with $k_{FeOnCu} > k_{FeOnFe} > k_{CuOnFe} \gg k_{CuOnCu}$. Any metal species that are not adsorbed during the impregnation step will remain in solution in the pores of the alumina until evaporation of the solvent (5).

In earlier research,[15] we studied the kinetics of the adsorption of iron cations on the surface of the same alumina supports as used in this work, by measuring the change in concentration of these cations during an impregnation procedure. In these measurements, no desorption of metal cations could be detected when the metal concentration in the contacting solution decreased, which suggests that the desorption process is relatively slow compared to the adsorption (i.e., the metals are very stably adsorbed on the alumina). Therefore, we consider the metals to have large adsorption equilibrium constants, and the difference in behavior between the two metals to stem from strongly different adsorption rate constants. In these earlier measurements (on iron), the time needed to reach the adsorption equilibrium was found to be about 10 min.

Combining the obtained model parameters (Table 3) and this mechanistic explanation, the experimentally obtained distributions (Figure 2, left) can be explained: Due to the slow adsorption of copper on alumina, the dissolved copper species hardly deposit during impregnation and are thus allowed to spread homogeneously throughout the support until evaporation of the solvent. Only in the case where iron is present on the surface of the alumina (during simultaneous impregnation or sequential impregnation with iron added in the first step), some limited deposition of copper can occur, resulting in some very slight inhomogeneities that track the iron distributions (e.g., Figure 2, row 4). The distribution of iron is mainly determined by its strong adsorption directly on the negative alumina surface sites, which is in competition with the even stronger adsorption of protons on the same sites. The formation of iron-rich bands thus occurs, as iron only starts to deposit at a high rate after a sufficient amount of protons are removed by adsorption on the outer parts of the alumina microspheres. The stronger shielding effects of Cl^- ions slow this adsorption of iron, which results in more diffuse iron distributions made from the $FeCl_3$ precursor. The adsorption of iron on deposited copper also is significant, as it adds another way for the iron to deposit early, as evidenced by the earlier and more pronounced iron band formation in simultaneous impregnation (Figure 2, row 1) and especially in sequential impregnation with iron in the second step (Figure 2, row 3).

4. CONCLUSIONS

In this work, the processes taking place during incipient wetness impregnation synthesis of bimetallic iron oxide/copper oxide @γAl_2O_3 microspheres have been elucidated, taking into account both the nanoparticle sizes and the distributions of both metals throughout the macroscopically shaped support. When both metals are added in a single impregnation step, the copper remains homogeneously distributed while the iron will deposit in a very pronounced egg-white distribution. Impregnating both metals sequentially improves the homogeneity of the iron distribution only if iron is added first, while adding iron in the second step drastically limits the iron to the outer shell of the microspheres. Also the microscopic properties are affected, as far more iron oxide cluster formation occurs when iron is added as the second material. From these results, it can be concluded that iron is not only adsorbed directly on the alumina surface, but there is also deposition possible on previously deposited metal, which was confirmed via STEM-EDX. Both the acidification of the iron precursor solutions and the use of iron citrate complexes increase the homogeneity of iron distributions and decrease the formation of large iron clusters. It has to be noted that, due to their viscosity, the use of iron citrate precursors negatively impacts the loading precision of the materials. Additionally, the use of high acid concentrations during the second step of a sequential impregnation also decreases the homogeneity of both metals in the final material.

Based on these results, the processes taking place during impregnation can be identified as competitive adsorption of charged dissolved species (Fe/Cu cations, protons, and additional anions) in the impregnation solution. This adsorption can take place on either charged alumina sites or previously deposited metal (i.e., iron on iron, copper on copper, iron on copper, and copper on iron) and is affected by counterion shielding. Modeling these interactions, and optimizing this model using the experimental results, allowed us to quantify the relative importance of each of the interactions. It was found that the adsorption of copper on alumina surface groups and previously deposited copper is very slow, while the copper deposition on previously deposited iron species is sufficiently fast to be observable. The adsorption of iron on alumina surface groups is very fast, but is always in competition with the adsorption of protons on these same groups, resulting in egg-white iron band formation. The anions (Cl^- and NO_3^-) present in solution can shield the iron from interacting and thus somewhat counteract this band formation. The deposition of iron on previously deposited copper clearly occurs and results in faster and earlier deposition of the iron, shifting the egg-white band more to the exterior of the support material. (i) Increasing the proton concentration of the iron precursor, (ii) reducing the amount of negatively charged alumina groups on the support, and (iii) complexation of the iron species with citrate ligands, all reduce the deposition of iron during impregnation and increase the homogeneity of the iron throughout the support.

The model presented in this work can be used to accurately predict the material properties of bimetallic materials based on the precursors and supports, which is useful for the controlled synthesis of bimetallic materials for specific applications.

■ ASSOCIATED CONTENT

Supporting Information

The Supporting Information is available free of charge at https://pubs.acs.org/doi/10.1021/acsomega.2c06273.

Iron and copper loadings of all samples, determined by ICP-OES; PXRD measurements of all samples; full results of experimentally determined metal distributions (SEM−EDX) and modeled metal distributions; and STEM images with EDX point measurements of selected samples (PDF)

■ AUTHOR INFORMATION

Corresponding Author

Bram Seynnaeve − *Industrial Catalysis and Adsorption Technology, Department of Materials Textiles and Chemical Engineering, Ghent University, 9000 Ghent, Belgium;*

https://doi.org/10.1021/acsomega.2c06273
ACS Omega 2022, 7, 41796−41803

orcid.org/0000-0002-0916-5253;
Email: Bram.Seynnaeve@Ugent.be

Authors

Jeroen Lauwaert − *Industrial Catalysis and Adsorption Technology, Department of Materials Textiles and Chemical Engineering, Ghent University, 9000 Ghent, Belgium;* orcid.org/0000-0003-2781-3477

Pascal Van Der Voort − *Center for Ordered Materials, Organometallics and Catalysis, Department of Chemistry, Ghent University, 9000 Ghent, Belgium;* orcid.org/0000-0002-1248-479X

An Verberckmoes − *Industrial Catalysis and Adsorption Technology, Department of Materials Textiles and Chemical Engineering, Ghent University, 9000 Ghent, Belgium;* orcid.org/0000-0003-2309-4874

Complete contact information is available at: https://pubs.acs.org/10.1021/acsomega.2c06273

Notes

The authors declare no competing financial interest.

■ ACKNOWLEDGMENTS

The author acknowledges support of the FWO-SBO project PLASMACATDESIGN (grant number S001619N). J.L. is a postdoctoral fellow of the Research Foundation Flanders (12Z2221N). Pieter Vermeir is acknowledged for the ICP-OES analysis.

■ REFERENCES

(1) Munnik, P.; de Jongh, P. E.; de Jong, K. P. Recent Developments in the Synthesis of Supported Catalysts. *Chem. Rev.* **2015**, *115*, 6687−6718.

(2) Seynnaeve, B.; Folens, K.; Krishnaraj, C.; Ilic, I. K.; Liedel, C.; Schmidt, J.; Verberckmoes, A.; Du Laing, G.; Leus, K.; Van Der Voort, P. Oxygen-rich poly-bisvanillonitrile embedded amorphous zirconium oxide nanoparticles as reusable and porous adsorbent for removal of arsenic species from water. *J. Hazard. Mater.* **2021**, *413*, No. 125356.

(3) Sharma, G.; Kumar, A.; Sharma, S.; Naushad, M.; Prakash, R.; Alothman, Z. A.; Tessema, G. Novel development of nanoparticles to bimetallic nanoparticles and their composites: A review. *J. King Saud Univ. Sci.* **2019**, *31*, 257−269.

(4) Wang, D.; Li, Y. Bimetallic Nanocrystals: Liquid-Phase Synthesis and Catalytic Applications. *Adv. Mater.* **2011**, *23*, 1044−1060.

(5) Alonso, D. M.; Wettstein, S. G.; Dumesic, J. A. Bimetallic catalysts for upgrading of biomass to fuels and chemicals. *Chem. Soc. Rev.* **2012**, *41*, 8075−8098.

(6) Choi, H.; Al-abed, S. R.; Agarwal, S.; Dionysiou, D. D. Synthesis of Reactive Nano-Fe/Pd Bimetallic System-Impregnated Activated Carbon for the Simultaneous Adsorption and Dechlorination of PCBs. *Chem. Mater.* **2008**, *20*, 3649−3655.

(7) Alexeev, O. S.; Gates, B. C. Supported bimetallic cluster catalysts. *Ind. Eng. Chem. Res.* **2003**, *42*, 1571−1587.

(8) Gawande, M. B.; Goswami, A.; Felpin, F.-X.; Asefa, T.; Huang, X.; Silva, R.; Zou, X.; Zboril, R.; Varma, R. S. Cu and Cu-Based Nanoparticles: Synthesis and Applications in Catalysis. *Chem. Rev.* **2016**, *116*, 3722−3811.

(9) Loza, K.; Heggen, M.; Epple, M. Synthesis, Structure, Properties, and Applications of Bimetallic Nanoparticles of Noble Metals. *Adv. Funct. Mater.* **2020**, *30*, No. 1909260.

(10) Lu, J.; Elam, J. W.; Stair, P. C. Synthesis and Stabilization of Supported Metal Catalysts by Atomic Layer Deposition. *Acc. Chem. Res.* **2013**, *46*, 1806−1815.

(11) Wong, A.; Liu, Q.; Griffin, S.; Nicholls, A.; Regalbuto, J. R. Synthesis of ultrasmall, homogeneously alloyed, bimetallic nanoparticles on silica supports. *Science* **2017**, *358*, 1427−1430.

(12) Ding, K.; Cullen, D. A.; Zhang, L.; Cao, Z.; Roy, A. D.; Ivanov, I. N.; Cao, D. A general synthesis approach for supported bimetallic nanoparticles via surface inorganometallic chemistry. *Science* **2018**, *362*, 560−564.

(13) Jamkhande, P. G.; Ghule, N. W.; Bamer, A. H.; Kalaskar, M. G. Metal nanoparticles synthesis: An overview on methods of preparation, advantages and disadvantages, and applications. *J. Drug Delivery Sci. Technol.* **2019**, *53*, No. 101174.

(14) Espinosa-alonso, L.; De Jong, K. P.; Weckhuysen, B. M. Effect of the Nickel Precursor on the Impregnation and Drying of γ -Al 2 O 3 Catalyst Bodies: A UV−vis and IR Microspectroscopic Study. *J. Phys. Chem. C* **2008**, *112*, 7201−7209.

(15) Seynnaeve, B.; Lauwaert, J.; Vermeir, P.; Van Der Voort, P.; Verberckmoes, A. Model-based control of iron- and copper oxide particle distributions in porous γ -Al 2 O 3 microspheres through careful tuning of the interactions during impregnation. *Mater. Chem. Phys.* **2021**, *276*, No. 125428.

(16) Hao, X.; Spieker, W. A.; Regalbuto, J. R. A further simplification of the revised physical adsorption (RPA) model. *J. Colloid Interface Sci.* **2003**, *267*, 259−264.

(17) Haber, J.; Block, J. H.; Delmon, B. Manual of methods and procedures for catalyst characterization (Technical Report). *Pure Appl. Chem.* **1995**, *67*, 1257−1306.